Phase retrieval for undersampled broadband images

J. R. Fienup

ERIM International, Inc., P.O. Box 134008, Ann Arbor, Michigan 48113-4008

Phase-retrieval algorithms have been used for wave-front sensing to determine the aberrations of an optical system from system point-spread functions (blurred images of point sources). Previously, computationally efficient algorithms were developed and applied to data from the Hubble Space Telescope [Appl. Opt. **32**, 1737 (1993); Appl. Opt. **32**, 1747 (1993)], but those algorithms, which employ analytic expressions for the gradient of an error metric, required narrow-band light and adequately sampled images. Generalizations of those phase-retrieval algorithms, which accommodate broadband light, allow for undersampled images, permit fitting of multiple images simultaneously, and have a flexible description of the aberrations, are described in this study. © 1999 Optical Society of America [S0740-3232(99)00207-0]

OCIS codes: 100.5070, 010.7350, 220.4840, 120.5050, 100.0100, 110.4980, 110.6770.

1. INTRODUCTION

The most common way to measure the aberrations of an optical system is to use an interferometer, but sometimes circumstances do not permit the use of interferometry. For example, after the Hubble Space Telescope (HST) was launched into orbit it was not practical to return it to Earth for interferometric measurements to determine its aberrations. Instead, phase-retrieval algorithms were used to determine its aberrations.[1–6] These algorithms employ one or more images of unresolved points (stars) taken through the aberrated system and find an aberration to impose on a computer model of the pupil function that predicts a blurred image consistent with the measured data.

In our previous work[2,3] we developed computationally efficient phase-retrieval algorithms that depended on the ability to propagate a wave front back and forth between the pupil and the detector plane. This allowed the entire gradient of an error metric to be computed with just two propagation calculations, irrespective of the number of unknown phase parameters. Unfortunately, that approach required that the images be coherent—that they be taken through narrow-band spectral filters and that they be sampled finely enough by the CCD array detector to Nyquist sample the optical field. This limited us to using images taken through narrow-band filters of wavelengths longer than 500 nm for the HST's Planetary Camera, so many of the available images from the Planetary Camera could not be used. There were no spectral filters transmitting wavelengths longer than the 1.667 μm required for the Wide-Field Camera, so these algorithms could use none of the images from the Wide-Field Camera.

In this paper new, generalized phase-retrieval algorithms that formally handle the cases of undersampled imagery and broadband light are derived. They involve using a more complicated and more complete forward model of the image formation process and deriving gradients for an error metric consistent with that model. Section 2 gives the forward model and the expressions for the derivatives. Various combinations of phase-error descriptions are possible, including polynomial and point-by-point (nonparametric) phase, single or multiple images optimized simultaneously, and phases that can be either the same or different for different images. Beside recovering phase, it is also possible to optimize over and to reconstruct other system parameters, such as the amplitude in the pupil plane.

Section 3 gives an example of phase retrieval by means of this approach on computer-simulated data. It also shows an example of the effect of using an insufficient number of wavelengths to adequately characterize the broadband light and indicates the robustness of the solution to noise. Section 4 gives conclusions.

2. GENERALIZED PHASE-RETRIEVAL ALGORITHMS

We first formulate a forward model of the aberrated optical system and detection process, then define an error metric or cost function that measures the difference between the predictions of the model and the measured data, and finally derive an analytic expression for the gradient of the error metric with respect to the unknown parameters for which we wish to solve. We can then incorporate this analysis into a conventional gradient-based nonlinear optimization algorithm to solve for the unknown parameters.

A. Forward Model
It is well known that the relationship between the optical field (wave front) in the pupil plane of a telescope and the field in the detector (image) plane is basically a Fourier transform.[7] For the HST's Wide-Field/Planetary Camera, for the highest accuracy it is also necessary to account for the fact that there is an obscuration at an additional plane that is not conjugate to the entrance pupil[2,3];

however, for simplicity in this paper we will treat only the case of the Fourier relationship. We may measure multiple images, and each of them could be at the same, or at different, focal positions and positions within the field of view. If there are field-dependent phase errors, then each image could have different phase errors, although the difference will usually reside only in the lowest-order terms. To allow for broadband light, we must explicitly use a wavelength-dependent model of the wave front. Using the discrete Fourier transform, computed with a fast Fourier transform (FFT), a model for the kth wave front of wavelength λ_l in the detector plane is

$$G_{lk}(p, q) = \left(\frac{\lambda_l}{\lambda_o}\right)\sum_{mn} A_l(m, n)$$
$$\times \exp\left[i\frac{\lambda_o}{\lambda_l}\phi_{ok}\left(\frac{\lambda_o}{\lambda_l}m, \frac{\lambda_o}{\lambda_l}n\right)\right]$$
$$\times \exp\left[-i2\pi\left(\frac{mp}{M} + \frac{nq}{N}\right)\right], \quad (1)$$

where l is the index over wavelength; k is the index over the different images; λ_o is a reference wavelength; A_l is the aperture function (which scales with wavelength); ϕ_{ok} is the phase error for the kth wave front at wavelength λ_o; and M and N are the array length and width, respectively, over which the FFT is computed. The kth point-spread function (PSF) at the lth wavelength is the squared magnitude of $G_{lk}(p, q)$.

A disadvantage of employing Eq. (1) is that it involves interpolating both the aperture function and the phase function to resample them differently for each wavelength. An alternative is the transform

$$G_{lk}(p, q) = \left(\frac{\lambda_o}{\lambda_l}\right)\sum_{mn} g_{lk}(m, n)$$
$$\times \exp\left[-i2\pi\left(\frac{mp}{M_l} + \frac{nq}{N_l}\right)\right], \quad (2)$$

where

$$g_{lk}(m, n) = A_o(m, n)\exp\left[i\frac{\lambda_o}{\lambda_l}\phi_{ok}(m, n)\right] \quad (3)$$

is the kth optical field in the pupil at the lth wavelength and $A_o(m, n)$ is the aperture function and $\phi_{ok}(m, n)$ is the phase error, both for a fixed wavelength λ_o. In this version of the transform, one performs the interpolation by varying, according to wavelength, the length of the FFT in each of the two dimensions, according to

$$\frac{1}{M_l} = \frac{\Delta u \, \Delta x}{\lambda_l z_f} = \frac{1}{M_o}\frac{\lambda_o}{\lambda_l} \quad (4)$$

and similarly for N_l, where Δx is the sample spacing in the pupil plane ($x = m\Delta x$), Δu is the sample spacing of $G_{lk}(p, q)$ in the detector plane ($u = p\Delta u$), z_f is the focal length, and M_o is the FFT length for wavelength λ_o. To allow for efficient computations of the FFT, we choose a set of wavelengths λ_l such that the FFT lengths M_l and N_l are highly composite numbers. When dealing with measured data that is undersampled, we choose a finer

sample spacing Δu for $G_{lk}(p, q)$ than for the sample spacing of the CCD detector array.

We model the phase error as

$$\phi_{ok}(m, n) = \sum_{jd=2}^{J1} a_{jd,k}Z_{jd}(m, n)$$
$$+ \sum_{js=J1+1}^{J} a_{js}Z_{js}(m, n) + \phi_{opp}(m, n), \quad (5)$$

where $Z_{jd}(m, n)$ are the $J1$ Zernike polynomials (or some other basis set) that may differ for each of the K wave fronts, Z_{js} are the polynomials that are the same for all the wave fronts, $a_{jd,k}$ and a_{js} are their respective coefficients, and $\phi_{opp}(m, n)$ is a point-by-point (nonparametric) phase map, needed for higher-order phase errors, which we assume here is the same for all wave fronts.

We model the detected intensity for the kth PSF as

$$I_k(p, q) = \text{grid}(p, q)\sum_{l=1}^{L} S_l|G_{lk}(p, q)|^2 * D(p, q), \quad (6)$$

where S_l is the spectral response at the lth wavelength and the convolution with $D(p, q)$ represents the integration over the area of a CCD pixel. The function $\text{grid}(p, q)$ is the sampling function, an array of delta functions separated by the detector sample spacings. The convolution in the equation above is performed at a finer sampling rate than the detector sample spacing for the case of undersampled data. Recall that we choose M_l and N_l to be highly composite numbers by adjusting the wavelengths λ_l. We can do this while keeping the same effective spectral properties by making appropriate adjustments in the value of the S_l.

Another possibility would be to allow for the object being extended, rather than an unresolved point. This case would be handled by a generalization of the phase-diversity algorithm.[8,9]

B. Error Metric
The error metric (or cost function or objective function) that we choose to minimize is the mean-squared error

$$E^2 = K^{-1}\sum_{k=1}^{K} \Phi_k^{-1}\sum_{pq} W_k(p, q)\text{grid}(p, q)$$
$$\times \left\{\alpha_k\left[\sum_{l=1}^{L} S_l|G_{lk}(p, q)|^2 * D(p, q)\right]^{1/2}\right.$$
$$\left. - |F|_k(p, q)\right\}^2, \quad (7)$$

where K is the number of PSF's used in the optimization, Φ_k is the weighted energy of the kth PSF, $W_k(p, q)$ is a weighting function that allows for reducing or excluding the effects of bad CCD pixels, $|F|_k(p, q)$ is the square root of the measurement at CCD pixel (p, q), and α_k is a factor used to normalize the energy of the modeled PSF to match that of the measured PSF.

Several other error metrics could be used. A particularly appropriate one would follow from a maximum-likelihood estimator, which depends on the noise model.

C. Analytic Gradients

To determine the unknown parameters (such as phase errors) by optimizing (minimizing) the error metric over the set of unknown parameters, it is valuable to have easily computable, analytic expressions for the partial derivatives of the error metric with respect to the parameters. Then one can avoid computing the derivatives by finite-difference methods, which are computationally expensive when the number of unknown parameters is large. Previously,[2] it was shown how all the partial derivatives (the entire gradient) can be computed with two propagations (FFT's) for the case of monochromatic light. In this section we generalize that computation to multiple wavelengths, multiple PSF's, and undersampled data.

Let β be a parameter of the pupil-plane optical field, $g_{lk}(m, n)$. Taking the partial derivative of the error metric with respect to β, we have

$$
\frac{\partial E^2}{\partial \beta} = K^{-1} \sum_{k=1}^{K} \alpha_k{}^2 \Phi_k{}^{-1} \sum_{pq} W_k(p, q)\mathrm{grid}(p, q)
$$

$$
\times \left\{ 1 - \frac{|F|_k(p, q)}{\alpha_k \left[\sum_{l=1}^{L} S_l |G_{lk}(p, q)|^2 * D(p, q) \right]^{1/2}} \right\}
$$

$$
\times \sum_{l=1}^{L} S_l \left[\frac{\partial |G_{lk}(p, q)|^2}{\partial \beta} * D(p, q) \right]. \quad (8)
$$

Using the fact that

$$
\frac{\partial |G_{lk}(p, q)|^2}{\partial \beta} = \left(\frac{\lambda_o}{\lambda_l}\right) G_{lk}{}^*(p, q) \sum_{mn} \frac{\partial g_{lk}(m, n)}{\partial \beta}
$$

$$
\times \exp\left[-i 2\pi \left(\frac{mp}{M_l} + \frac{nq}{N_l} \right) \right] + \text{c.c.}, \quad (9)
$$

where c.c. denotes the complex conjugate of the expression that precedes it, and

$$
\frac{\partial |G_{lk}(p, q)|^2}{\partial \beta} * D(p, q)
$$

$$
= \left(\frac{\lambda_o}{\lambda_l}\right) \sum_{mn} \frac{\partial g_{lk}(m, n)}{\partial \beta} \sum_{p'q'} G_{lk}{}^*(p', q')
$$

$$
\times \exp\left[-i 2\pi \left(\frac{mp'}{M_l} + \frac{nq'}{N_l} \right) \right]
$$

$$
\times D(p - p', q - q') + \text{c.c.}, \quad (10)
$$

and changing the order of the three spatial summations, we find that

$$
\frac{\partial E^2}{\partial \beta} = -K^{-1} \sum_{l=1}^{L} S_l \left(\frac{\lambda_o}{\lambda_l}\right) \sum_{k=1}^{K} \alpha_k{}^2 \Phi_k{}^{-1}
$$

$$
\times \sum_{mn} \frac{\partial g_{lk}(m, n)}{\partial \beta} (g_{lk}{}^D)^*(m, n) + \text{c.c.}, \quad (11)
$$

where

$$
(g_{lk}{}^D)^*(m, n)
$$

$$
= \sum_{p'q'} \exp\left[-i 2\pi \left(\frac{mp'}{M_l} + \frac{nq'}{N_l} \right) \right] G_{lk}{}^*(p', q')
$$

$$
\times \sum_{pq} D(p - p', q - q') W_k(p, q)\mathrm{grid}(p, q)
$$

$$
\times \left\{ \frac{|F|_k(p, q)}{\alpha_k \left[\sum_{l=1}^{L} S_l |G_{lk}(p, q)|^2 * D(p, q) \right]^{1/2}} - 1 \right\}. \quad (12)
$$

We can think of $g_{lk}{}^D(m, n)$ as the pupil-plane field quantities that tell us how the current estimates of the fields disagree with the measured data. The most computationally intensive aspects of computing the KL functions $g_{lk}{}^D(m, n)$ are the KL propagations (FFT's) used to compute the detector-plane fields $G_{lk}(p, q)$ and the final KL FFT's in Eq. (12). Note that there are only K convolutions with $D(p, q)$, the CCD detector pixel area, and K cross correlations with $D(p, q)$. Since $D(p, q)$ is nonzero only over the area of a CCD pixel, the convolution and the cross correlation with $D(p, q)$ is faster if performed directly rather than by Fourier techniques, and it is done at the finer sample spacing. The cross correlation arises from the convolution found in the detection process because of the reversal of the order of the summations. Its effect is to spread the information from a single sample defined on $\mathrm{grid}(p, q)$ associated with a particular CCD pixel over all the samples associated with the area of that CCD pixel at the finer sample spacing of the computed field $G_{lk}(p, q)$.

Note the similarity between the above expression for the gradient of the error metric and the expression in Appendix B of Ref. 3 that includes the effects of jitter. This similarity arises because the effects of both jitter and CCD-pixel integration are convolutional. By incorporating a known jitter spread function into the kernel $D(p, q)$ we could include jitter in this analysis as well. This new formulation allows for finite spectral bandwidth and undersampling as well, which was not allowed previously.[2,3]

The partial derivatives of $g_{lk}(m, n)$, the pupil-plane fields, with respect to a variety of (β) parameters are given as follows:

$$
\frac{\partial g_{lk}(m, n)}{\partial a_{jd,k1}} = i\left(\frac{\lambda_o}{\lambda_l}\right) g_{lk}(m, n) Z_{jd}(m, n) \delta(k, k1), \quad (13)
$$

$$
\frac{\partial g_{lk}(m, n)}{\partial a_{js}} = i\left(\frac{\lambda_o}{\lambda_l}\right) g_{lk}(m, n) Z_{js}(m, n), \quad (14)
$$

$$\frac{\partial g_{lk}(m,n)}{\partial \phi_{\mathrm{pp}}(m1,n1)} = i\left(\frac{\lambda_o}{\lambda_l}\right) g_{lk}(m1,n1)\delta(m,m1)\delta(n,n1),$$

$$(15)$$

$$\frac{\partial g_{lk}(m,n)}{\partial \operatorname{Re}[g_{l1,k1}(m1,n1)]}$$

$$= \delta(m,m1)\delta(n,n1)\delta(l,l1)\delta(k,k1), \qquad (16)$$

$$\frac{\partial g_{lk}(m,n)}{\partial \operatorname{Im}[g_{l1,k1}(m1,n1)]}$$

$$= i\,\delta(m,m1)\delta(n,n1)\delta(l,l1)\delta(k,k1), \qquad (17)$$

$$\frac{\partial g_{lk}(m,n)}{\partial A_o(m1,n1)}$$

$$= \exp\left[i\frac{\lambda_o}{\lambda_l}\phi_{ok}(m1,n1)\right]\delta(m,m1)\delta(n,n1), \quad (18)$$

where δ is the Kronecker delta function, given by

$$\delta(m,m1) = \begin{cases} 1, & m = m1 \\ 0, & m \neq m1 \end{cases}. \qquad (19)$$

If we were to have a point-by-point phase map that was different for each PSF, then the partial derivative of g with respect to it would be like Eq. (15), but with an additional product with $\delta(k,k1)$.

Inserting these relations into the expression for the partial derivative of the error metric yields the derivatives

$$\frac{\partial E^2}{\partial a_{jd,k1}} = 2K^{-1}\alpha_{k1}{}^2\Phi_{k1}{}^{-1}\sum_{mn} Z_{jd}(m,n)\sum_{l=1}^{L} S_l\left(\frac{\lambda_o}{\lambda_l}\right)^2$$

$$\times \operatorname{Im}[g_{lk1}(m,n)(g_{lk1}{}^D)^*(m,n)], \qquad (20)$$

$$\frac{\partial E^2}{\partial a_{js}} = 2K^{-1}\sum_{mn} Z_{js}(m,n)\sum_{k=1}^{K}\alpha_k{}^2\Phi_k{}^{-1}\sum_{l=1}^{L} S_l\left(\frac{\lambda_o}{\lambda_l}\right)^2$$

$$\times \operatorname{Im}[g_{lk}(m,n)(g_{lk}{}^D)^*(m,n)], \qquad (21)$$

$$\frac{\partial E^2}{\partial \phi_{\mathrm{opp}}(m1,n1)} = 2K^{-1}\sum_{k=1}^{K}\alpha_k{}^2\Phi_k{}^{-1}\sum_{l=1}^{L} S_l\left(\frac{\lambda_o}{\lambda_l}\right)^2$$

$$\times \operatorname{Im}[g_{lk}(m1,n1)(g_{lk}{}^D)^*(m1,n1)],$$

$$(22)$$

$$\frac{\partial E^2}{\partial g_{l1,k1}(m1,n1)}$$

$$\equiv \frac{\partial E^2}{\partial \operatorname{Re}[g_{l1,k1}(m1,n1)]} + i\frac{\partial E^2}{\partial \operatorname{Im}[g_{l1,k1}(m1,n1)]}$$

$$= -2K^{-1}\sum_{k=1}^{K}\alpha_k{}^2\Phi_k{}^{-1}\sum_{l=1}^{L} S_l\left(\frac{\lambda_o}{\lambda_l}\right)g_{lk}{}^D(m1,n1), \quad (23)$$

$$\frac{\partial E^2}{\partial A_o(m1,n1)}$$

$$= -2K^{-1}\sum_{k=1}^{K}\alpha_k{}^2\Phi_k{}^{-1}\sum_{l=1}^{L} S_l\left(\frac{\lambda_o}{\lambda_l}\right)$$

$$\times \operatorname{Re}\left\{\exp\left[i\frac{\lambda_o}{\lambda_l}\phi_{ok}(m1,n1)\right](g_{lk}{}^D)^*(m1,n1)\right\}. \quad (24)$$

We also find that

$$\frac{\partial E^2}{\partial \alpha_{k1}} = 2K^{-1}\Phi_{k1}{}^{-1}\sum_{pq} W_{k1}(p,q)\mathrm{grid}(p,q)$$

$$\times \left\{\alpha_{k1}\left[\sum_{l=1}^{L} S_l|G_{lk}(p,q)|^2 * D(p,q)\right]^{1/2}\right.$$

$$\left. - |F|_{k1}(p,q)\right\}$$

$$\times \left[\sum_{l=1}^{L} S_l|G_{lk}(p,q)|^2 * D(p,q)\right]^{1/2}. \qquad (25)$$

Setting this partial derivative to zero and solving, we find that the optimum value of the normalization parameter, for given values of the other parameters, is

$$\alpha_{k1\mathrm{opt}} = \frac{\displaystyle\sum_{pq} W_{k1}(p,q)\mathrm{grid}(p,q)|F|_{k1}(p,q)\left[\displaystyle\sum_{l=1}^{L} S_l|G_{lk}(p,q)|^2 * D(p,q)\right]^{1/2}}{\displaystyle\sum_{pq} W_{k1}(p,q)\mathrm{grid}(p,q)\displaystyle\sum_{l=1}^{L} S_l[|G_{lk1}(p,q)|^2 * D(p,q)]}. \qquad (26)$$

(In practice we hold α_k constant for most of our calculations and update it only occasionally.)

3. COMPUTER SIMULATION EXAMPLE

Our previous algorithms[2,3] were limited to using images from the HST's Planetary Camera taken through narrowband filters of wavelengths greater than 500 nm. To test the generalized phase-retrieval algorithm, we simulated PSF's through the camera's F555W spectral filter, which is wideband and (centered at 555 nm) includes significant spectral content below 500 nm. We simulated the effect of the filter by using five wavelengths, as given in Table 1. For simplicity we assume that both the spectral emissivity of the source star and the spectral sensitivity of the CCD detectors are independent of wavelength. For each of two PSF's, we simulated phase errors across the pupil, using the values of the Zernike coefficients given in the first row (labeled True) in Table 2. Both PSF's have the same aberrations except for the fourth Zernike polynomial, that of focus. The modified Zernike polynomials that we used are those given in Table 17 of Ref. 3. The simulated pupil functions included the obscurations of the HST's Optical Telescope Assembly, including the secondary mirror, the spiders holding the secondary mirror, and three circular bolts that hold the primary mirror in place. For each focal position and at each of the five wavelengths, we computed finely sampled monochromatic PSF's, using a 256×256 FFT. For each focal position, we added the S_l-weighted intensities of the five monochromatic PSF's to arrive at a finely sampled polychromatic PSF. We then summed over 2×2 groups of pixels to form 128×128 arrays that simulate the effects of spatial integration and undersampling by the CCD elements. Figure 1 shows the polychromatic PSF's and examples of the monochromatic PSF's. Note that the finest fringe structures in the monochromatic PSF's are washed out in the polychromatic PSF's. Effects due to diffraction from

edges of the pupils are suppressed by the combined effects of the wideband light and the undersampling by the CCD. Nevertheless, all the large-scale structure in the PSF remains. This structure results from the geometrical-optics effects of the aberrations in combination with the gross features of the pupil function. These smoothed PSF's still retain the information necessary for successful phase retrieval.

We performed several phase-retrieval experiments, retrieving the phase error jointly from these two simulated PSF's.

When we ran the phase-retrieval algorithm, described above, using the same five wavelengths as in the data simulation and using the true solution as an initial estimate, it stayed at the true solution.

When we ran the algorithm starting with an incorrect aberration estimate, it would converge to the true solution or not, depending on the starting estimate. For example, if the focus terms of our initial estimate were both positive or both negative (i.e., PSF's on the same side of the focus rather than on opposite sides of the focus), then it would not converge. It is easy to see how the algorithm would prevent the estimate from approaching the true solution in such a case. When the estimated focus term has the wrong sign, to get to the correct sign the focus estimate would have to pass through zero to approach the correct value. But for these highly out-of-focus PSF's, a computed PSF with the correct magnitude but the incorrect sign of the focus term will match the measured PSF better than a tightly focused PSF with zero for the focus term. Consequently, the algorithm will not allow the focus term to go near zero, so it cannot pass through zero to approach the correct sign. Then the algorithm will stagnate at a local minimum without finding a solution consistent with the measured data. For this reason the algorithm has a certain capture range: Initial estimates too far from the true solution may never converge to the true solution. This can be overcome by use of a number of initial estimates with different focus terms.

In one series of experiments we used the initial estimate given in the row labeled Initial in Table 2. When we used the same five wavelengths to simulate the forward imaging problem during the reconstruction, we obtained the values shown in the row labeled Rec. 5 in Table 2. The largest deviation from the true solution in this case was 0.005 waves, for the focus term of the second PSF. When we used just a single wavelength, 555 nm, to simulate the forward imaging problem as though it were monochromatic during the reconstruction, we obtained

Table 1. Simulated Wavelengths and Spectral Response for WF/PC F555W Filter

l	λ_l (nm)	S_l
1	472.5	0.78
2	516.0	0.91
3	562.5	0.82
4	609.0	0.50
5	656.0	0.18

Table 2. Values of Zernike Coefficients[a]

Case	Focus A 4A	Focus B 4B	Astigmatism 5	Astigmatism 6	Coma 7	Coma 8	Triangular Coma 9	Triangular Coma 10	Spherical 11
True	1.500	−0.750	0	0	0	0.010	−0.020	0.010	−0.300
Initial	1.200	−0.400	0	0	0	0	0	0	−0.250
Rec. 5[b]	1.499	−0.755	0.000	0.002	0.001	0.008	−0.020	0.010	−0.299
Rec. 1[c]	1.473	−0.531	0.002	−0.004	0.008	0.021	−0.016	0.001	−0.314

[a] Values are given in waves rms at a wavelength of 500 nm.
[b] Reconstruction with five wavelengths.
[c] Reconstruction with only one wavelength.

(a)

(c)

(b)

(d)
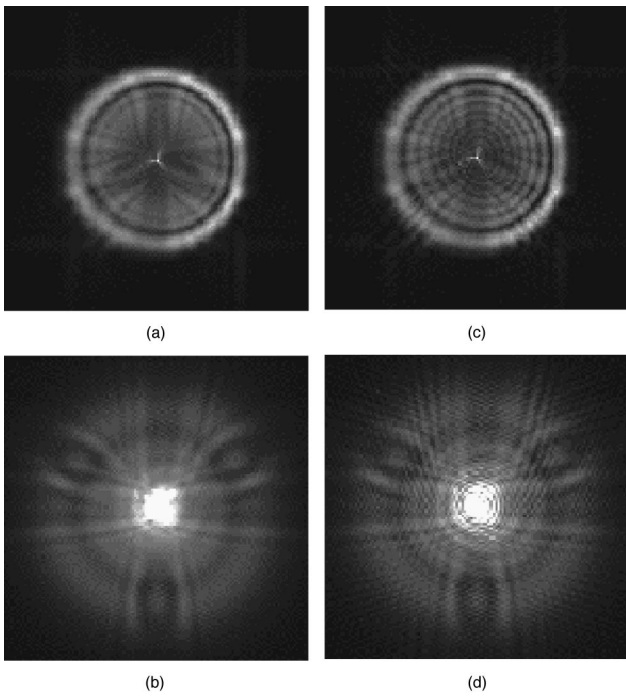
Fig. 1. Simulated PSF's. (a) Polychromatic PSF with +1.5 waves (rms) defocus, (b) polychromatic PSF with −0.75 waves defocus, (c) monochromatic PSF with +1.5 waves defocus, (d) monochromatic PSF with −0.75 waves defocus.
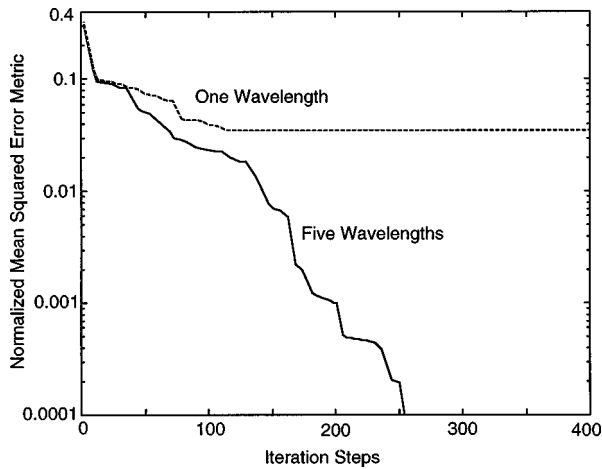
Fig. 2. Normalized error as a function of iteration number. Upper curve, calculated with a monochromatic PSF calculation; lower curve, calculated with a polychromatic PSF calculation.

the values shown in the row labeled Rec. 1 in Table 2. The largest deviation from the true solution in this case was 0.224 waves, for the focus term of the second PSF. In this case the algorithm had stagnated without arriving at a solution. We would know that the algorithm stagnated because the reconstructed PSF's differed from the measured PSF's by substantial amounts. Figure 2 shows plots of the error metric as a function of iteration number for both cases. The squared error metric, given by Eq. (7), was 0.303 for the initial estimate. For the polychromatic reconstruction the final error metric, after 300 steps, was 0.0001. For the monochromatic reconstruction the final error metric, after 400 steps, was 0.034. Here we define a step to be one evaluation of the error

metric. (There were typically three to six evaluations of the error metric for each evaluation of the gradient of the error metric.) This experiment demonstrates the importance of modeling the PSF's with their proper spectral bandwidth.

To demonstrate the effect of low light levels on the accuracy of the aberration estimation, we imposed various amounts of Poisson noise on the two simulated PSF's. Figure 3 shows two extreme cases. Since the error depends on the starting estimate, we chose to determine the best-case error by starting the algorithm with the true solution and letting the algorithm converge to a noisy solution that is more consistent with the noisy PSF's. Figure 4 shows the residual error in the phase estimate as a function of light level. This error is the square root of the sum of the squares of the errors in the reconstructed Zernike polynomial coefficients, in waves. The scale at the bottom of Fig. 4 is given in terms of both the total

(a)

(c)

(b)

(d)
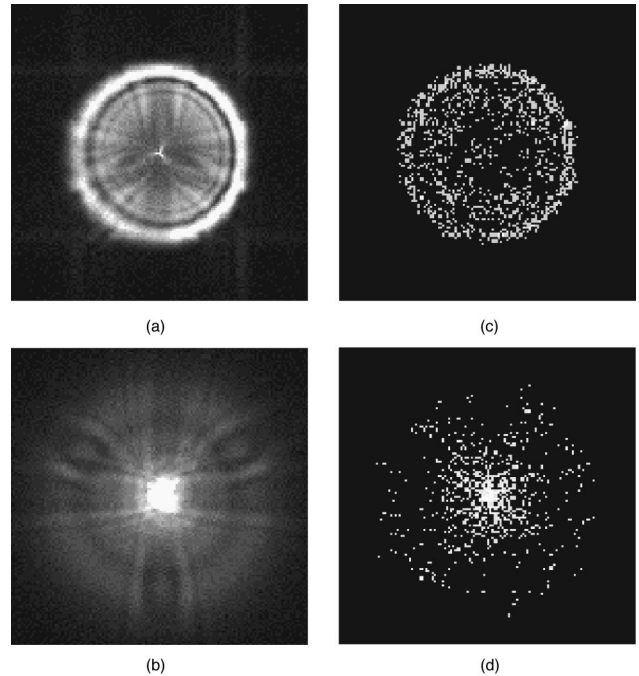
Fig. 3. PSF's with photon noise. (a), (b) 1,000,000 total photons; (c), (d) 1000 total photons.
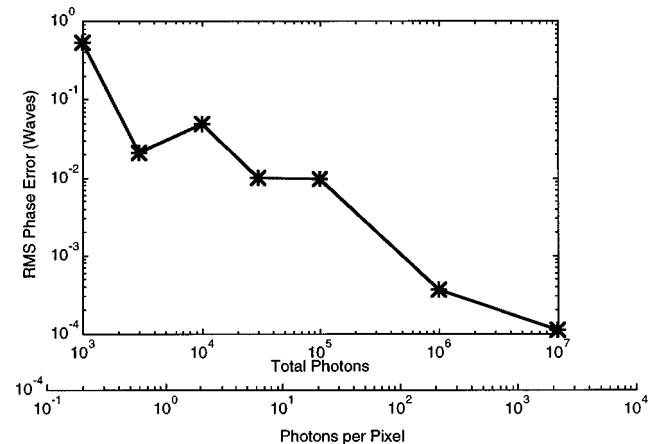
Fig. 4. Residual rms phase error versus light level.

number of photons per PSF and the number of photons per pixel. The first PSF is spread over a circle of roughly 70 pixels in diameter, or roughly 5000 pixels in area. For these highly defocused PSF's the rms wave-front error was approximately 0.01 waves when there were just a few photons per pixel.

4. CONCLUSIONS

In this paper we have generalized previous gradient-based phase-retrieval algorithms,[2,3] employing efficient calculation of analytic gradients, to the cases of wideband light, undersampling by the CCD detector, and multiple PSF's. The new formulation can also incorporate known telescope jitter. It has been shown, with a short-wavelength, wideband simulation of the Hubble Space Telescope PSF's, that successful phase retrieval can be obtained despite wideband light and undersampled PSF's. These effects obscure most of the fine fringelike detail resulting from edge diffraction that is present in oversampled, monochromatic PSF's; however, they do not destroy the gross features predicted by geometrical optics, which may explain how our algorithm can still succeed. Another explanation is that the particular aberrations that we investigated could be described by a modest number of low-order polynomial coefficients; it would be interesting to see how well this approach works with random, high-order phase errors. Having reduced the requirements for both spatial coherence of the light (by including the incoherent convolution with the CCD pixels) and temporal coherence (by widening the optical bandwidth), we now have efficient phase-retrieval algorithms that can operate on light with greatly reduced coherence. The more complicated forward model of the imaging process requires additional computation, and the number of FFT's per iteration is proportional to both the number of wavelengths simulated and the number of PSF's being fitted simultaneously.

The generalized algorithm was demonstrated to have improved accuracy and robustness to stagnation on wideband data when employing a wideband model as compared with a monochromatic model. Another interesting question would be, If we had our choice between selecting a narrow-band filter and a wideband filter through which to collect the data, which would we choose? If the signal-to-noise ratio (SNR) were high for the monochromatic data, then we would expect them to be the better data. However, it is possible that, in a light-starved regime, the greater SNR for the wideband images would make them yield superior results. This might be especially true when the images are undersampled, since the fine details of the monochromatic images would be washed out any-way. One would also like to know what the optimum defocus is as a function of spectral bandwidth, aberration complexity, SNR, and undersampling ratio. From earlier work with HST data[3] we know that some defocusing is better than none. However, one would be at a disadvantage to defocus to the extent that the SNR per pixel becomes too low.[10]

These algorithms could be further generalized to accommodate more-complicated optical systems, as was done previously.[2,3] Other generalizations could include the use of other error metrics, such as one arising from maximum-likelihood estimation, and operation with extended objects, as is accomplished with phase diversity.[8,9]

ACKNOWLEDGMENT

REFERENCES

1. *Space Optics for Astrophysics and Earth and Planetary Remote Sensing, 1991*, Vol. 19 of 1991 OSA Technical Digest Series (Optical Society of America, Washington, D.C., 1991).
2. J. R. Fienup, "Phase-retrieval algorithms for a complicated optical system," Appl. Opt. **32**, 1737–1746 (1993).
3. J. R. Fienup, J. C. Marron, T. J. Schulz, and J. H. Seldin, "Hubble Space Telescope characterized by using phase-retrieval algorithms," Appl. Opt. **32**, 1747–1768 (1993).
4. C. Roddier and F. Roddier, "Combined approach to Hubble Space Telescope wave-front distortion analysis," Appl. Opt. **32**, 2992–3008 (1993).
5. J. E. Krist and C. J. Burrows, "Phase-retrieval analysis of pre- and post-repair Hubble Space Telescope images," Appl. Opt. **34**, 4951–4964 (1995).
6. R. G. Lyon, J. E. Dorband, and J. M. Hollis, "Hubble Space Telescope faint object camera calculated point-spread functions," Appl. Opt. **36**, 1752–1765 (1997).
7. J. W. Goodman, *Introduction to Fourier Optics* (McGraw-Hill, San Francisco, Calif., 1968).
8. R. A. Gonsalves, "Phase retrieval and diversity in adaptive optics," Opt. Eng. **21**, 829–832 (1982).
9. R. G. Paxman and J. R. Fienup, "Optical misalignment sensing and image reconstruction using phase diversity," J. Opt. Soc. Am. A **5**, 914–923 (1988).
10. J. R. Fienup, B. J. Thelen, R. G. Paxman, and D. A. Carrara, "Comparison of phase diversity and curvature wavefront sensing," in *Adaptive Optical Systems Technologies*, D. Bonaccini and R. K. Tyson, eds., Proc. SPIE **3353**, 930–940 (1998).
11. J. R. Fienup, "Phase retrieval for multiple undersampled polychromatic images," in *Signal Recovery and Synthesis*, Vol. 11 of 1998 Technical Digest Series (Optical Society of America, Washington, D.C., 1998), pp. 41–43.
12. J. R. Fienup, "White-light phase retrieval," presented at the Annual Meeting of the Optical Society of America, Baltimore, Md., October 4–9, 1998.